Orientale Ejecta at the Apollo 14 Landing Site Implies a 200-million-year Stratigraphic Time Shift on the Moon

Stephanie C. Werner[1] , Benjamin Bultel[1] , Tobias Rolf[1], and Vera Assis Fernandes[1,2,3]
[1] Centre for Earth Evolution and Dynamics (CEED), Department of Geosciences, University of Oslo, PO 1028 Blindern, NO-0315 Oslo, Norway
stephanie.werner@geo.uio.no
[2] Department of Earth and Environmental Sciences (DEES), University of Manchester, M13 9PL Manchester, UK
[3] Museum für Naturkunde Leibniz-Institut für Evolutions- und Biodiversitätsforschung. D-10115 Berlin, Germany

Abstract

Detailed spectral mapping, cratering statistics, and impact basin ejecta column estimates document a new and very different stratigraphic relationship for the Apollo 14 landing site. We observe a resurfacing event in the crater size–frequency distribution in agreement with a single blanketing layer. Using the crater size–frequency distribution, we determine two relative ages (cumulative crater frequencies) that match those observed for the Imbrium and Orientale basins, respectively. The pattern and strength of resurfacing and morphological distinction by spectral features suggest the top layer to be about 10–25 m thick. We propose that this top layer at the Apollo 14 landing site is Orientale basin ejecta above Imbrium basin ejecta. Such stratigraphy reattributes the (majority of) Apollo 14 samples to Orientale rather than to Imbrium basin and implies that Orientale basin is about 3.92 Gyr old, 200 million years older than previously suggested. The youngest lunar basin thus formed at the onset, rather than amid, of recorded mare volcanism. This time shift also changes constraints on early planetary and solar system processes, such as the intensity of impact bombardment, and pleads for revision of the crater-statistics-based surface ages of other planetary bodies.

1. Introduction—The Apollo 14 Landing Site

Gilbert (1893) was the first to describe the Fra Mauro formation and Imbrium basin morphology and geological setting. He interpreted radial grooves and furrows pointing toward the centers of the Mare Imbrium inside the Imbrium basin and of the basin itself to be the ejecta blanket of the Imbrium basin. This relationship eventually prompted the selection of the Apollo 14 landing site, located ∼50 km from the Fra Mauro crater beyond the rim of Imbrium basin (Gilbert 1893; Wilhelms 1987). The traditional view of the Moon is that the Imbrium basin and its ejecta dominate the lunar nearside stratigraphically and compositionally, and thus many samples collected at the Fra Mauro formation where the Apollo 14 mission landed allegedly date to Imbrium basin formation (Stadermann et al. 1991).

The age of 3.92 Ga commonly suggested for Imbrium basin formation (e.g., Fernandes et al. 2013; Merle et al. 2014; Nemchin et al. 2021) appears ubiquitously for highland material samples obtained at other landing sites (e.g., of the Apollo 15, 16, and 17 and Luna 20 missions; Swindle et al. 1991; Fernandes et al. 2013; Nemchin et al. 2021). Therefore, an alternative interpretation suggests that, based on vicinity association of the respective landing site to a specific basin, several basins (Serenitatis, Nectaris, Crisium, and a few intercalated basins), including Imbrium, could have formed in a very short time interval around 3.92 Ga ago (e.g., Tera et al. 1973). This period therefore appears to have a short, spike-shaped increase in projectile flux, also termed *late heavy bombardment*. Different disciplines provided supporting and opposing arguments, such as crater statistics for a monotonic impactor flux decay (e.g., Neukum et al. 1975), dynamical simulations for permissibility of a late heavy bombardment (Wetherill 1975), or isotopic evidence for and against such a terminal lunar cataclysm (Tera et al. 1973; Turner et al. 1973; Tera et al. 1974). Although we know the sample collection coordinates on the Moon, the sample provenance is often unresolvable and much disputed since the early 1970s. On the Moon, primarily crater formation moves material at different scales that hinder interpretation because of (1) global basin ejecta deposition and (2) impact gardening by subsequently formed smaller craters. These processes formed the majority of lunar rocks, which are breccia composed of clasts whose provenance is unknown.

The Imbrium basin is the third-youngest basin on the Moon, succeeded by Schrödinger and Orientale basins, according to superposed crater densities (e.g., Fassett et al. 2012). The Imbrium basin is nearly 1300 km in diameter and the most prominent impact basin on the nearside of the Moon. Crisium (older) and Orientale (younger) basins follow in size (Neumann et al. 2015). If the stratigraphic section at the Apollo 14 landing site were strictly composed of the Imbrium ejecta blanket, then rocks with the same age as Imbrium basin formation cover large areas of the Moon, because of the global dispersal of ejecta. In the following, we keep this line of arguments but provide observations that suggest Orientale basin, being the youngest basin, to be the source of both a likely global, topmost ejecta layer and the 3.92 Ga aged samples.

2. Methods and Materials

2.1. Spectral Investigation

Moon Mineralogy Mapper Instrument (Green et al. 2011) is a hyperspectral imager in the visible to near-infrared range covering 430–3000 nm with 85 spectral channels and with a spatial resolution of 140 m pixel^{-1}. We use image cube data of two optical periods: M3G20090207T003331 (OP1B) and

M3G20090110T154845 (OP1A). The level-2 calibration of the cubes includes a photometric and thermal correction, provided by the Planetary Data System (NASA PDS, https://pds.nasa.gov). We removed an assumed continuum spectrum based on tie points at 770, 1618, and 2576 nm following Zhang et al. (2016). Guided by the Apollo 14 samples, which suggest the presence of minerals such as pyroxene and feldspar, we formulated spectral criteria (Table 1) to enable the assessment of the mineral composition in the remote-sensing data. We only assess relative abundances, which were normalized for display in the detection maps. We show red-green-blue color-composite maps, for example, the criterion BD930, BD1250, and BD1900 in the red, green, and blue channel, so that the resulting color represents the proportional presence of the respective relative abundance identified in accordance with the three selected spectral criteria.

Table 1
Spectral Criteria

Name	Spectral Criterion Definition	Display Color
BD930:	$1 - \dfrac{1.75 * R(930) + 0.25 * R(1030)}{R(750) + R(1409)}$	Red in Figure 1(a)
BD1250:	$1 - \left(\dfrac{R(1249)}{\frac{R(770) - R(1469)}{(1469 - 770) * (1249 - 770) + R(770)}} \right)$	Green in Figure 1(a)
BD1250r	$1 - \dfrac{2 * R(1230)}{R(1110) + R(1429)}$	Blue in Figure 1(c)
BD1900:	$1 - \left(\dfrac{R(1898)}{\frac{R(2497) - R(1409)}{(2497 - 1409) * (1898 - 1409) + R(1409)}} \right)$	Blue in Figure 1(a); red in Figure 1(b)
BD2020	$1 - \left(\dfrac{1.5 * R(2018) + 0.5 * R(2297)}{R(1429) - R(2576)} \right)$	Green in Figure 1(b)
BD2300	$1 - \left(\dfrac{R(2377)}{\frac{R(2576) - R(1579)}{(2576 - 1579) * (2297 - 1579) + R(1658)}} \right)$	Blue in Figure 1(b)

Note. $R(X)$ is the reflectance at wavelength X (in nm)

2.2. Crater Statistics

For crater statistics, we determined the size–frequency distribution of craters on Kaguya Terrain Camera images (Haruyama et al. 2008) downloaded from the SELENE Data Archive (SELENE Data Archive, JAXA, https://darts.isas.jaxa.jp/planet/pdap/selene/), processed with the Integrated Software for Imagers and Spectrometers (ISIS3, USGS, http://isis.astrogeology.usgs.gov/) and integrated in ArcGIS. We used high-resolution images (listed in Table A1) to create both morning and evening mosaics to perform the crater counts. The spatial image resolution of 10 m pixel^{-1} allows us to confidently analyze craters with diameters greater than 200 m. The crater diameters are determined using three points at the crater rim with CraterTools (Kneissl et al. 2011). While delineating the counting unit, we avoided areas of secondary-crater clusters.

For the data presentation, we use cumulative crater size–frequency distribution (CSFDs) plots, and we use crater-production function best fits to define a normalized crater density (e.g., N_{cum} ($D \geqslant 1$ km)), which provides the relative age. We use an 11th-order polynomial in double logarithmic scale that describes the crater-production function as defined by Neukum et al. (2001). Best fits are determined using the Levenberg–Marquardt nonlinear least-squares algorithm (Levenberg 1944; Marquardt 1963). We utilize the differential plot presentation of the count results as aid for the identification of resurfacing events. We applied the in-built resurfacing correction of the CraterStats tool (Michael & Neukum 2010) required for best fits in cumulative distribution plots to obtain the crater frequency for the crater population after resurfacing occurred. Moreover, we used empirical saturation lines to identify the validity limit for the age determination at the smaller crater diameter range.

2.3. Estimated Basin Ejecta Accumulation at Landing Sites

We compute the distribution of basin ejecta across the lunar surface using a scaling law (Zhu et al. 2015; Rolf et al. 2017) of the form $d_i(\alpha) = d_i^{max} \left(\frac{\alpha}{\alpha_{r,i}} \right)^B$. Here d_i is the ejecta thickness originating from basin i at angular distance (α) from the basin center, $\alpha_{r,i}$ is the angular radius of basin i, and $d_i^{max} = f(\alpha_{r,i})$ is the maximum deposit thickness, assumed to be found at the basin rim. The exponent B controls the decrease of ejecta thickness with increasing distance. We chose $B = -2.9$, in agreement with the range of values used in previous studies ($-3.2 \leqslant B \leqslant -2.6$; e.g., McGetchin et al. 1973; Housen et al. 1983; Fassett et al. 2011; Zhu et al. 2015). For the maximum

deposit thickness, we make use of its constrained value at the Orientale basin rim ($d_{Or}^{max} = 2.9^{+0.3}_{-0.3}$ km; Fassett et al. 2011), but also lower estimates exist (e.g., $d_{Or}^{max} = 0.9^{+0.5}_{-0.5}$ km; Xie & Zhu 2016). We assume that d_i^{max} scales with the basin volume and that all material within the basin cavity is excavated and deposited only outside the basin. To derive the basin volume, we approximate each basin as a half-ellipsoid whose volume scales with basin depth. We convert observed basin radii (Neumann et al. 2015) into basin depth according to a depth–diameter relationship for lunar basins (Dibb & Kiefer 2015). Inside a newly formed impact basin, the stratigraphy is reset, $d_i(\alpha < \alpha_{r,i}) = 0$, but the new basin may subsequently be filled with ejecta from younger basin formation events. These equations assume radial-symmetric deposition of ejecta and do not account for the curvature of the lunar surface, discontinuation in the ejecta deposit, or any alteration such as erosion and mixing between different ejecta layers due to secondary or other subsequent impact cratering (but see discussion in Section 3.5).

During impact basin formation, vast amounts of ejected material deposit across the lunar surface, forming time-sorted, kilometer-thick stacks of ejecta layers (Wilhelms 1987). Our predicted stratigraphy of each landing site is the result of the cumulated ejecta layers (Table 2). The basin formation sequence (Fassett et al. 2012) dictates the order of ejecta emplacement, with the younger layer deposited on top of older contributions. Only the sequence of basin formation matters here, not actual basin ages. Changing the scaling law parameters never alters the position of basin deposits in the sequence, but it affects the thickness of the layers. Previous estimates (e.g., McGetchin et al. 1973) underestimated layer thickness because of smaller assumed basin diameters, lower ejecta material volume (e.g., Pike 1974), and the choice of exponent B, already indicated by Moore et al. (1974). The estimated stratigraphy differs in layer thicknesses for different parameters in detail (Table A2), but the obtained thicknesses of Orientale and Imbrium ejecta at the Apollo 14 site are relatively robust across the studies since the calibration work of Fassett et al. (2011).

2.4. Compilation and Updating of Sample Ages

We compiled sample ages (Table 7.3.1 of Basaltic Volcanism Study Project 1981 and references therein), for which we corrected ^{40}Ar/^{39}Ar step-heating and ^{87}Rb/^{87}Sr age data. We

Table 2
Layer Thickness of Several Basins Contributing to the Strata at the Landing Sites

	A-14	A-16	A-17	L-20
SOUTH POLE–AITKEN	145	147	…	…
NUBIUM	755	122	…	…
MENDEL-RYDBERG	12	10	…	…
HUMORUM	299	48	…	…
SERENITATIS	111	240	…	…
SMYTHII	9	28	46	…
NECTARIS	67	1085	205	…
CRISIUM	39	138	825	…
IMBRIUM	519	204	361	83
SCHRÖDINGER	<0.5	1	<0.5	1
ORIENTALE	27	11	6	4
Σ	1983	2034	1443	88

Note. Nomenclature: A-XX = Apollo mission XX; L-XX = Luna mission XX. All values are in units of meters. The last row is the cumulative value. Ellipsis dots indicate that the respective basin would not be seen in the stratigraphy anymore, because the stratigraphy was reset by a subsequent impact.

reevaluated and interpreted these data using updated values for the ^{40}K decay (Renne et al. 2011) and ^{87}Rb decay constants (Nebel et al. 2011). For the $^{40}Ar/^{39}Ar$ ages, additional consideration was given to changes in the age of the neutron flux monitor (or ^{39}Ar monitor) used and inserted in the same irradiation setup as the samples investigated, and for which ages were recalculated in Renne et al. (2011). Some literature references (e.g., Stadermann et al. 1991) do not include step-heating data, and hence reevaluation of the age is not possible. Several of the ^{39}Ar monitors used in the 1970s, while different researchers in different laboratories around the world were developing the $^{40}Ar/^{39}Ar$ method, have been discontinued, resulting in age corrections based only on the new values for the ^{40}K decay constants. Following all possible updates and apparent age recalculation per heating step for each sample, we plotted data using Isoplot (Ludwig 2003) to acquire the corresponding updated age spectrum and respective statistics (e.g., mean squared weighted deviation (MSWD) and probability (P)) to assess the reliability of the updated age. For the $^{40}Ar/^{39}Ar$ ages reported in the literature, there is a wide range by which the age changed with the update in the ^{40}K decay constants. Ages can increase from 1% to 13% (mostly 3%–4%); however, in some cases the age decreased by 1%–2% (Fernandes et al. 2014). The actual relative age correction depends on the combination of the decay constant correction and the updated age of the ^{39}Ar monitor used in the irradiation of the samples analyzed. Thus, the correction of ages reported in the literature is a case-by-case situation, and just applying a general single correction value is insufficient for updating literature sample ages. Similarly, $^{87}Rb/^{87}Sr$ ages reported in Neukum (1983) have been corrected for the current ^{87}Rb decay constant value of Nebel et al. (2011) and replotted using Isoplot (Ludwig 2003), enabling the extraction of an updated $^{87}Rb/^{87}Sr$ age. For the past years, different research groups

using state-of-the-art instrumentation (e.g., $^{40}Ar/^{39}Ar$, $^{87}Rb/^{87}Sr$) and new analytical techniques (e.g., in situ U/Pb, Re-Os) have acquired more reliable ages, which are also considered. Table A3 lists modern and updated ages for Apollo 14 samples, including updated ages previously reported in Basaltic Volcanism Study Project (1981) for comparison.

3. Observations and Results

3.1. Spectral and Geological Mapping

We investigated the Fra Mauro formation at the Apollo 14 landing site based on spectral data and mosaicked image data. We used a combination of spectral criteria (Table 1) and identified feldspar and low-calcium pyroxene at the actual landing site coordinates characterized by absorptions near 990 nm, near 1230 nm, and near 2050 nm. We outlined the Apollo 14 geological reference unit (Landing-Site Unit) according to the joint low-calcium pyroxene and feldspar signatures, a typical composition for highland rocks (e.g., Warren 1985). We also observe patches characterized by absorptions near 950 nm and near 2000 nm indicative of a lower calcium content in the pyroxene compared to the overall Landing-Site Unit. The Mare Unit, the basalt plain west of the Landing-Site Unit, is characterized by absorptions near 1000 nm and near 2100 nm indicative of a pyroxene higher in calcium. We show the spatial distribution of different compositions in the resulting color maps representing combinations of several spectral criteria (Figure 1). For example, displaying the detections according to the spectral criteria BD930, BD1250, and BD1900 in the red, green, and blue (RGB) channels, the Landing-Site Unit features in green, the patches in purple, and the Mare Unit in orange (Figure 1(a)).

We further investigated the variability around 2000 nm with the criteria BD1900, BD2020, and BD2300, displayed again in RGB channels shown in Figure 1(b). Superposing the maps onto the image data reveals that the patches (purple in Figure 1(a), white in Figure 1(b)) correlate with some but not all impact craters. Due to the compositional difference, these patches represent either mixtures of the surface material and underlying strata or only material of an excavated deeper layer. However, they cannot be mixtures with the mare basalt observed in the Mare Unit, which has the highest Ca content, while we observed the lowest Ca content for the patches.

To investigate further the feldspar signature, we used a simple band criterion (BD1250r, Table 1), alternative to the BD1250 criterion, in an attempt to reduce the noise and avoid the interference of the large absorption near 1000 nm present for the Mare Unit. Although the noise reduction is limited, both the Mare Unit and compositional patches associated with some impact craters show very low values compared to the remaining part of the mapped area (Figure 1(c)). This absorption is not restricted to the Landing-Site Unit and is not sufficient to define its boundary. Consequently, we utilized the other spectral criteria and morphology to define the geological unit that we use for crater statistics. Only in combination with an additional spectral criterion, which shows variations in the absorption near 2000 nm (Figure 1(b)), can we capture the extent of the Landing-Site Unit based on spectral and morphological features. We have delineated this geological reference unit for the landing site in order to measure its CSFD and eventually for cratering chronology model calibration.
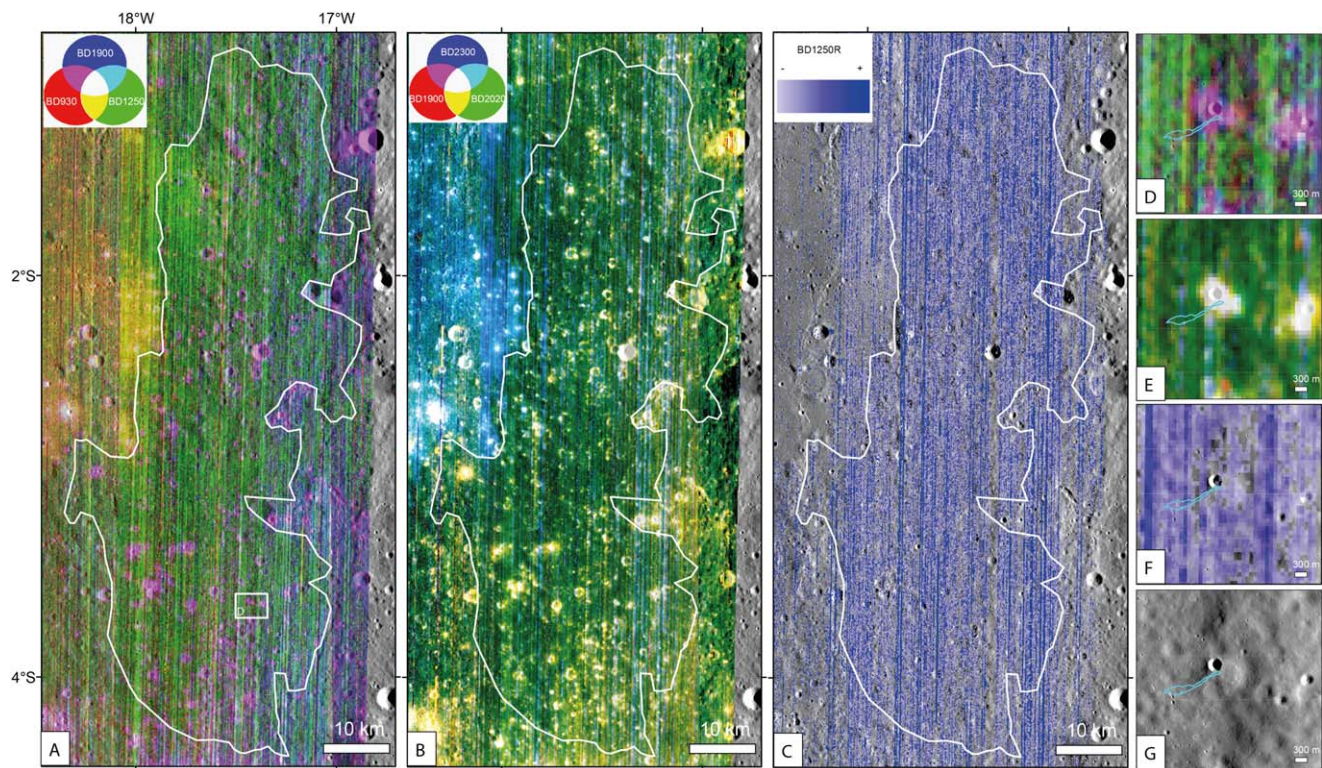
Figure 1. Spectral analysis of the Apollo 14 landing site using M^3 data. (a) Map depicting the results of the spectral data analysis based on the combination of three spectral criteria (see Table 1) into a color scheme of red-green-blue (R: BD930; G: BD1250; B: BD1900). The defining characteristics of the Landing-Site Unit show up in green in the spectral criteria map for the surfaces rich in low-calcium pyroxene and feldspar (typical highland rocks) and in purple for surfaces corresponding to material with pyroxene poorer in calcium and lack of a feldspar signature. We outlined the morphologically and spectrally defined unit in white for crater statistics. (b) Map showing the combined spectral criteria that evaluates the variations of the absorption near 2000 nm (R: BD1900; G: BD2020; B: BD2300). (c) Map of the relative feldspar abundance based on the absorption band at 1250 nm. (d, e, f, g) Zoom-in to Cone crater and the astronaut track (cyan line) as outlined in panel (a) (white rectangle in panel (a)). The zoom-in for panel (a) is shown in panel (d), for panel (b) in panel (e), for panel (c) in panel (f), and in panel (g) the panchromatic image data. Panel (d) shows the clear relationship between the ejecta Cone crater and spectral features (purple). The astronauts' track touches the rim of Cone crater in the center of the map.

3.2. Craters with Spectral Anomalies

The spectral maps show patches of surface material corresponding to potentially fresh impact craters and their ejecta, for example, at Cone crater (Turner et al. 1971). The spectral signature of these patches suggests the presence of pyroxenes poorer in calcium and the lack of the feldspar signature, when compared to the overall Landing-Site Unit. These spectral differences are due neither to the relative material immaturity caused by space-weathering or temperature variations nor to mixing of mare and highland materials, but to real compositional variations related to the Ca content of the pyroxenes. As shown by Ogawa et al. (2011), space weathering does not influence the position of the centers of absorptions, nor does the space-weathering process cause a reduction of Ca in the pyroxene or remove the feldspar signature. Figure 1(b) clearly identifies variation of absorption centers around 2000 nm indicative for variations in the Ca content of the pyroxene.

We evaluated the sizes of those craters that possess such a spectral anomaly and therefore reached into the deeper compositionally distinct stratum. We find that craters smaller than about 75 m in diameter are not associated with spectral anomalies and therefore formed only within the surficial top layer, not reaching into the compositionally different underlying layer. We use one-third of crater diameter as suggested by the maximum penetration depth of the transient-crater cavity as a measure for the layer depth (e.g., Prieur et al. 2017). Thus, the thickness of this top layer could be up to about 25 m, and at least 7.5 m considering an excavation depth of at least 1/10 the crater diameter as the lower limit. Only some of the larger craters feature this spectral deviation in the ejecta or in the inner crater walls. This demonstrates the excavation of material from a compositionally different, deeper (older) stratum and the layer beneath, for which we could not detect feldspar and its pyroxene has the lowest calcium content. This layer is at least 320 m thick. The fact that not all, larger, craters show the spectral feature requires them to have formed before the emplacement of the top layer, and they are now covered by the subsequently emplaced 10–25 m thick layer.

3.3. Comparison of Apollo 14 Remote-sensing and Sample Laboratory Spectra

Several laboratory spectra of Apollo 14 rock samples are accessible through the RELAB collection (NASA RELAB facility at Brown University, RELAB collection, http://www. planetary.brown.edu/relab/), shown in Figure 2. The astronauts walked across both spectrally identified units, which close to the landing module is spectrally representing the Landing-Site Unit (green in the Figure 1(a)) or coincides with the Cone crater ejecta similar to the spectrally different patches (purple in Figure 1(a)). Sample 14311, collected near the landing module, may correspond to ejected impact melt breccia and consists mostly of matrix (75%; Simonds et al. 1977). Sample 14310 is a KREEP-rich feldspathic basalt found
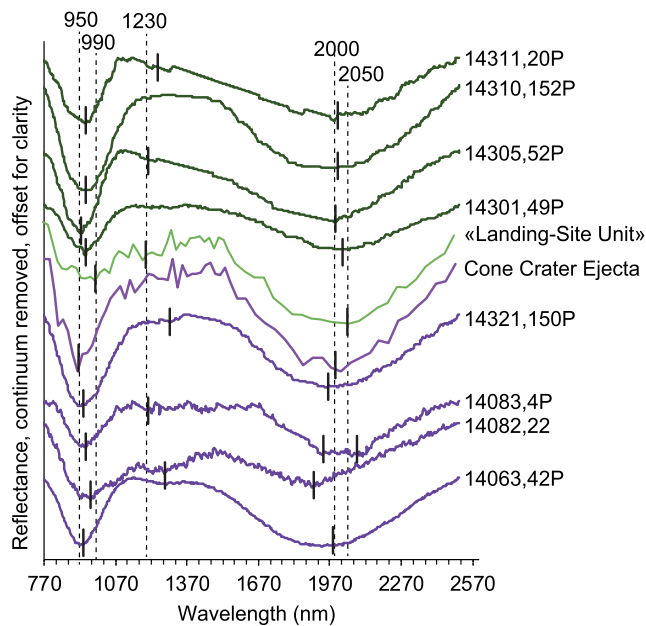
Figure 2. Comparison of laboratory sample and M^3 remote-sensing spectra. The two M^3 remote-sensing spectra represent the spectral features of the Landing-Site Unit (green) and the Cone crater ejecta blanket (purple). Sample spectra are plotted according to the collection sites, either in green when they were picked in the Landing-Site Unit on top of the plot or in purple when the collections sites are located on the Cone crater ejecta blanket at the bottom of the plot. Black short vertical lines indicate centers of absorptions. Dotted lines indicate centers of main absorptions seen on the spectral units at the Apollo 14 landing site.

separately without adhering matrix (Gancarz et al. 1972; Longhi et al. 1972). No absorption feature testifies of its feldspathic composition, despite its 60% feldspar content. Similarly, although sample 14310 has ∼30% of low-calcium pyroxene (including ∼10%–20% pigeonite) against 0% to ∼7% of high-calcium pyroxene, the absorptions near 1000 and 2000 nm indicate a rather intermediate Ca content. Therefore, we consider the spectrum registered in the database not representative of the sample. Sample 14305 is a clast-rich crystalline matrix breccia similar to sample 14321 (Simonds et al. 1977). Sample 14301 is a regolith breccia collected near the "Triplet craters" close to the landing site (Simonds et al. 1977). Sample 14321, called "Big Bertha," is a brecciated rock that could correspond to either of the two layers studied here but was collected at the rim of Cone crater (Simonds et al. 1977). Samples 14082 and 14083 are clast-rich impact melt breccia, and sample 14063 is a regolith breccia; all were collected close to Cone crater (Simonds et al. 1977). Sample 14082 has a high proportion of feldspar (54%–62% of the pheno-crystalline part) and does exhibit an absorption related to feldspar. Sample 14083 has broken off from 14082 but shows a different spectrum without feldspar and pyroxene with higher amounts of Ca. Sample 14063 is mostly composed of a matrix, and the crystalline part is dominated by feldspar (∼56%) and does exhibit a spectral feature near 1250 nm.

For comparison (Figure 2), we plot representative spectra of the two spectrally and compositionally different units derived from the M^3 remote-sensing data and those of the samples according to the spectral unit in which they were collected. The sample spectra have no clear systematic features and are not distinctive in correspondence to their collection sites. They show either absorptions near 1250 nm indicating feldspar

content independently of whether the sample lay on the Landing-Site Unit or Cone crater ejecta, or absorptions indicative for higher Ca content in the pyroxene than that of the Cone crater signal in M^3 data. No laboratory sample spectra of pure impact melt exist, and it is not possible to find a perfect match between M^3 spectra and library spectra. However, we cannot exclude firmly that some component from the layer beneath is present in some samples, related to variability in the absorptions near 1000 and 2000 nm. Because either all samples indicate a feldspathic component or their pyroxene shows high calcium content when we consider both the 1000 and 2000 nm absorptions, we suggest that the top layer seen in the M^3 data (corresponding to the Landing-Site Unit and shown in Figure 1(a) in green) is a better match to all the spectra acquired for Apollo 14 rocks.

3.4. Resurfacing History at the Apollo 14 Landing Site

Spectroscopic data suggest the excavation of a compositionally different material from a layer deeper than about 10–25 m. The local terrain at the Apollo 14 landing site is smooth and covered by regolith (Figure 1(g)). For further insight in the regional resurfacing history, we analyzed the newly derived crater statistics of the spectrally and morphologically defined Landing-Site Unit (Figure 3). When compared to a crater-production function for an unmodified geological unit (e.g., Neukum et al. 2001), this crater record reveals two episodes of resurfacing. The resurfacing processes can be distinguished based on kinks in the CSFD and by how the observed CSFD slope deviates from that of the crater-production function. The first kink emerges at about 950 m and marks one of the two events. This event is restricted in time, indicated by the offset in the crater frequencies between the surviving (larger) and subsequently formed (smaller) craters, but with the same distribution slope. Craters larger than marked by the onset of deviation (kink) measure the exposure of the original surface. Smaller craters measure the exposure of the new superposed surface layer, which accumulated craters only since the resurfacing event (Figure 3). This is a uniform and temporally restricted resurfacing event. The second kink occurs at about 500 m in diameter, where the observed CSFD slope shallows. For craters smaller than ∼500 m in diameter, the surface is at least in the so-called saturation equilibrium (e.g., Gault 1970; Xiao & Werner 2015), because the continuous resurfacing by steady formation of new craters erases smaller craters more readily. This crater population with diameters less than 500 m is inadequate for age determination based on crater statistics.

The cumulative crater frequencies, $N_{cum}(\geqslant 1\,km)$, we observe for the lower and upper strata are $0.028 \pm 0.003\,km^{-2}$ and $0.0099 \pm 0.0008\,km^{-2}$, respectively. The resurfacing was already observed previously and reported by Neukum et al. (1975). They described similarly a difference between the relative age derived from the total crater population defined by the cumulative crater frequency $N_{cum}(\geqslant 1\,km) = 0.044 \pm 0.003\,km^{-2}$ and the crater population of a topmost layer ($0.020 \pm 0.003\,km^{-2}$). Despite the observed resurfacing event, Neukum (1983) later derived an average crater frequency of $0.037 \pm 0.007\,km^{-2}$ for dating the Fra Mauro formation and the Imbrium basin. In contrast, Robbins (2014) never reported resurfacing, and his measured crater density ($0.0484 \pm 0.0054\,km^{-2}$) is the highest. These earlier studies used reference units including the coordinates of the Apollo 14 landing site, which differed in areal extent to the one defined in
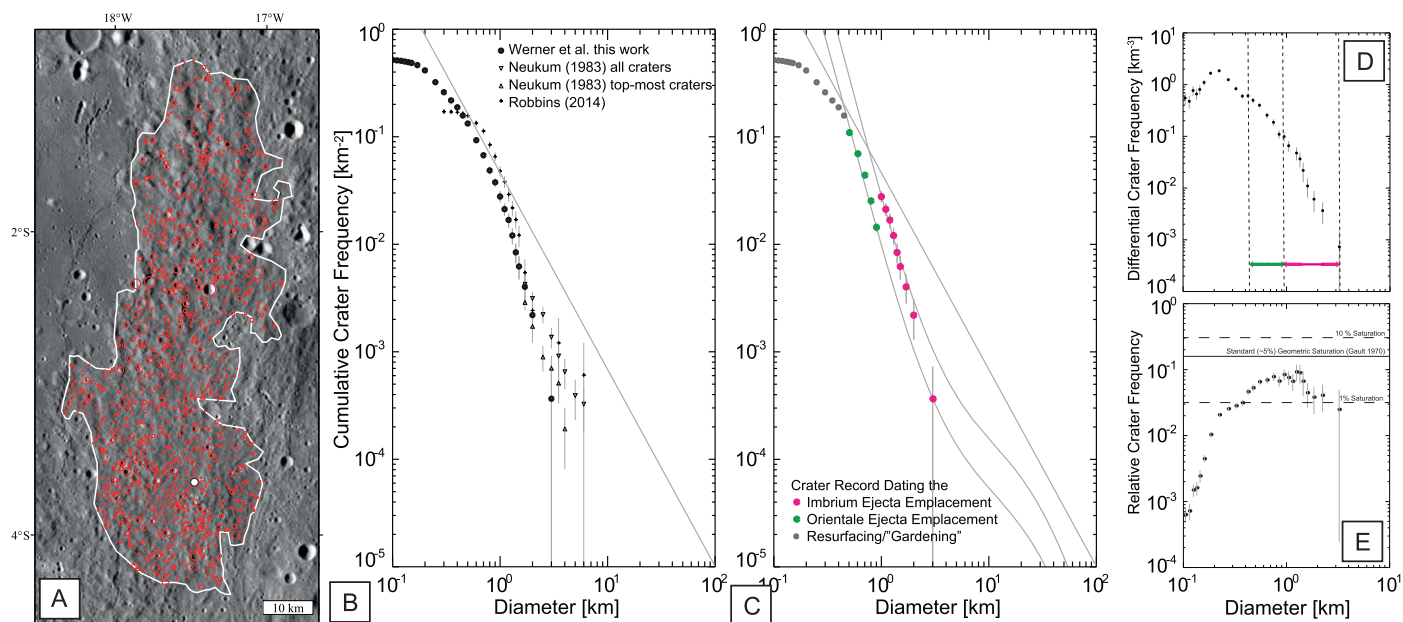
Figure 3. Crater statistics for the Apollo 14 landing site. (a) Image of the landing site area including the outline of the Landing-Site Unit according to the combined spectral and morphological data (white line); the white dot marks the landing site; craters are marked as red circles according to their diameters. North is up. (b) Crater size–frequency distributions (CFSD) for the craters observed in panel (a) and previous measurements (Neukum et al. 1975; Robbins 2014) for comparison; error bars show standard deviation. (c) The CFSD analysis: craters (magenta) measure the exposure of the original surface and date the Imbrium ejecta emplacement; craters (green) formed in the Orientale ejecta blanket and date its emplacement; craters (gray) may be in saturation equilibrium (Gault 1970) and are not used for dating. Gray curves indicate best-fit crater-production functions for the green and magenta colored sections or the crater-saturation equilibrium curve, respectively. (d) The CSFD in a differential instead of the cumulative histogram; colored bars mark the crater size range defining the fit ranges for age determination, and dashed lines mark the kinks. (e) The CSFD as the so-called relative crater frequency (with respect to a simple power law) and three levels of geometric saturation (1%, standard: ∼5%, 10%) after Gault (1970).

our study. The area investigated by Robbins (2014) has the largest extent.

3.5. Basins' Ejecta Deposition and Impact Gardening at Landing Sites

We reconstruct the stratigraphy of ejecta deposition for the Apollo 14, 16, and 17 and Luna 20 landing sites (Table 2). Both Imbrium and Orientale basins added ejecta to the stratigraphic columns of these landing sites, while the intermediate Schrödinger basin contributed only a negligible amount, mainly because it is substantially smaller in diameter and because of its greater distance to those landing sites. The contribution of Imbrium ejecta at these landing sites is on average at least 100 m, with about 500 m at the Apollo 14 site. The average thickness of the Orientale ejecta layer at these landing sites ranges between 5 and 27 m, being thickest at the Apollo 14 site (Table 2). The curvature of the lunar surface causes variations of estimated layer thicknesses compared to the here-assumed flat surface (e.g., Xie et al. 2020). Most prominently, distal ejecta may focus at the antipode of the impact location (Xie et al. 2020; Wieczorek & Zuber 2001), but the locations of the here-studied landing sites and basin centers are all scattered within the same hemisphere. A strong antipodal contribution from the South Pole–Aitken basin, the oldest basin in the sequence, may substantially alter the bottom of the stratigraphic column but does not strongly impact this study, which focuses on the most recent basin-forming events. Because of secondary cratering during emplacement of basin ejecta, Oberbeck (1975) suggested strong mixing of ejecta deposits and substrate materials. Accordingly, Orientale ejecta material would be strongly mixed with underlying strata and

may not even dominate the upper 20–30 m of the A-14 stratigraphic column (Oberbeck et al. 1974; Petro & Pieters 2004, 2006). This model prediction is in contrast to our observations of a spectrally distinct layer formed by the emplacement of Orientale ejecta and the observed local crater population at the Apollo 14 site. We suggest that the ejecta reaching this far, having a velocity of about 1.7–1.8 km s^{-1} for Orientale material according to Haskin et al. (2003), cannot be made of large particles that would produce secondary craters of a size comparable to the layer thickness. Therefore, the degree of mixing as suggested by Oberbeck (1975) is more limited, because it would require substantial secondary-crater formation during the ejecta emplacement even at large distances away from the basin rim.

Seismic erasure of small crater morphology as a result of basin formation (Kreslavsky & Head 2012) will not affect the crater record after Orientale formation, because it is the last basin-forming event; we also limited our study to craters larger than 500 m in diameter. Whether it may be a significant effect on the crater population formed in between earlier events, we are not able to judge, because we suggest that the Orientale-forming event caused the last global ejecta layer, covering previously formed craters. Several mapping studies of the near-field ejecta surrounding the Orientale basin indicate a non-radial-symmetric deposition of ejecta (Wu et al. 2019, and references therein), based on secondary-cratering patterns. This could suggest an oblique impact, and for small craters this implies lack of ejecta in the uprange direction. By direct modeling of ejecta distribution during oblique basin-scale impacts, Fernandes & Artemieva (2012) demonstrated that for the Orientale basin substantial ejecta material is also deposited in the uprange direction at the distance of the Apollo 14 site,

even though not equally in all radial directions. In support of far-reaching ejecta, Orientale basin ejecta have recently been identified at the Chang'E-4 landing site (Xiao et al. 2021), which lies farther away from Orientale than the Apollo 14 site.

Relative dating of lunar surfaces via crater size–frequency measurements uses craters that form after the basin ejecta emplacement, but each crater (irrespective of its size) causes further material comminution (regolith fragments formation; Housen et al. 1979) and its transport (impact gardening; Arvidson et al. 1975). The local turnover of strata due to continuous cratering occurs down to a depth comparable to two-thirds of the crater radius (Prieur et al. 2017). The combination of global-scale basin ejecta deposition and local cratering causes the complex history of the sampling sites. It also challenges the provenance interpretations of samples found at the landing sites, because samples could have originated from different strata and distant sources. At the young mare landing sites (i.e., Apollo 11, 12, and 15, and Luna 16 and 24), this is clearly observed in stray rocks that are much older than the mare units are. For example, Apollo 15 landed on a volcanic plain of Mare Imbrium with a prevalent age of about 3.3 Ga (e.g., Snape et al. 2019). However, the Apollo 15 sample collection comprises rocks that are older, such as Apollo 15 "KREEP basalts" 15382 and 15386, which have ages ranging from 3.85 to 3.89 Ga (Snape et al. 2019). These samples with (potentially local) highland origin could resemble Apollo 14 "high-Al" basalts (Neal & Kramer 2006). However, confusion is caused by the manifold nomenclature (Walker et al. 1973). Because of the correlation in age (compared to Apollo 14 samples) and resemblance to some Apollo 14 samples, Apollo 15 "KREEP basalts" could potentially link to the Apollo 14 landing site. Since these are samples of different composition and older compared to the Apollo 15 mare samples, it is clear that these boulders were transported to the Apollo 15 sampling site more recently than the emplacement of the plains by the mare volcanism less than 3.3 Ga ago. There are other Apollo 15 samples (15445, 15455), breccia with shocked norite clasts (Watkins & Kovach 1972), which are breccia distinguishably different from the Apollo 15 "KREEP basalt" samples 15382 and 15386. These breccia samples include many clasts that are very old (more than 4.3 Ga), cemented together within a matrix. The matrix material of sample 15455 was analyzed and indicated a recrystallization age of about 3.9 Ga (Ryder & Wood 1977). None of these rocks relate to the mare volcanic rocks constituting the Apollo 15 site, and it is unclear from where and how they were transported to the Apollo 15 landing site.

Concerning the remaining landing sites (Apollo 11 and 12, Luna 16 and 24), being located, similar to the Apollo 15 landing site, on young mare plains, any sample with significantly older ages would have been transported to the site after the respective mare volcanism occurred. That is, the transported material would sit on top of the lava plain as it is observed. These old rocks certainly have been moved much later (after the plains-forming volcanism) to the collection site. Hence, their source could have been anywhere on the lunar surface.

In recently formed craters at the Apollo 14 landing site, such as Cone crater, material transport is easily recognizable spectrally by the discriminable composition of materials excavated. Combining the sizes of spectrally distinct craters, crater statistics, and our estimated basin ejecta stratigraphy, we conclude that the Apollo 14 site surface exhibits a 10–25 m thick, compositionally and temporally distinguishable layer. This layer formed after the formation of the majority of craters

in the diameter range smaller than about 950 m. Unlike what earlier studies suggested (Chao et al. 1972; Ryder & Wood 1977), craters such as Cone crater penetrated compositionally stratified layers but did not reach the deeper underlying local bedrock. Hence, both the crater record and spectral information support the presence of a few-tens-of-meters-thick layer of deposited ejecta of one basin that formed after the Imbrium basin. Schrödinger and Orientale basins are the only candidates, but the ejecta contribution of Schrödinger is very small if at all present at this site (Table 2). Therefore, we suggest that Orientale basin is the source for the material in the observed thin top layer.

Our new crater size–frequency measurement shows one distinct resurfacing event. We suggest this event to be the emplacement of the Orientale basin ejecta blanket on top of the Imbrium basin proximal ejecta blanket. We can establish temporal constraints between the landing site and large young basins based on local crater statistics and crater frequencies representative of the formation age of the basins. The cumulative crater frequencies, $N_{cum}(\geqslant 1\,\mathrm{km})$, for the lower and upper strata observed are $0.028 \pm 0.003\,\mathrm{km}^{-2}$ and $0.0099 \pm 0.0008\,\mathrm{km}^{-2}$, respectively. Independent measurements (Fassett et al. 2012) of the cumulative crater frequency associated with Imbrium basin and Orientale basin result in values of $\sim 0.027 \pm 0.003\,\mathrm{km}^{-2}$ and $\sim 0.011 \pm 0.001\,\mathrm{km}^{-2}$, respectively. These two sets of values are identical within uncertainty (Figure 4). Therefore, we infer that the topmost layer is the ejecta blanket of Orientale basin, and below that there may be an at least 300 m thick ejecta layer of the Imbrium basin. By implication, it is uncertain whether actually any ejecta from Imbrium was sampled by the Apollo 14 mission.

3.6. Sample Ages

In the Apollo 14 sample collection, we find two dated sample types (Table A3, including references), clast-rich impact melt breccia with an age of around 3.92 ± 0.06 Ga (some including relic zircon grains as old as 4.35 Ga), and the second type, broadly described as feldspathic (sometimes brecciated) basalts covering a wide age range between 4.31 ± 0.17 Ga and 3.94 ± 0.03 Ga. However, many ages are recognized in subsamples of the same breccia and therefore must have reached the sampling site together and reflect the complex history of the source area. Nemchin et al. (2021) reviewed ages of impact-breccia samples across several landing sites with ages close to 3.92 Ga to derive the limits for the timing of the Imbrium basin formation to 3.922 ± 0.012 Ga. While we here use the ages according to the evaluation by Nemchin et al. (2021), we dispute the sample affiliation. Contrary to the Apollo 15 site, the Apollo 14 site presents a clear and simple stratigraphic relationship between Imbrium and Orientale ejecta deposits. The assumption remains in accordance with our stratigraphic results based on the estimated ejecta accumulation for several other landing sites (Apollo 16 and 17 and Luna 20; Table 2), showing the likelihood of finding samples with an age of ~ 3.9 Ga across the Moon. Orientale basin is the youngest large lunar basin, and its ejecta would therefore be superimposed onto any earlier-deposited basin ejecta. While the Fra Mauro formation and as such the Imbrium basin formed earlier, the top cover formed at 3.922 ± 0.012 Ga and thus dates the Orientale basin formation.
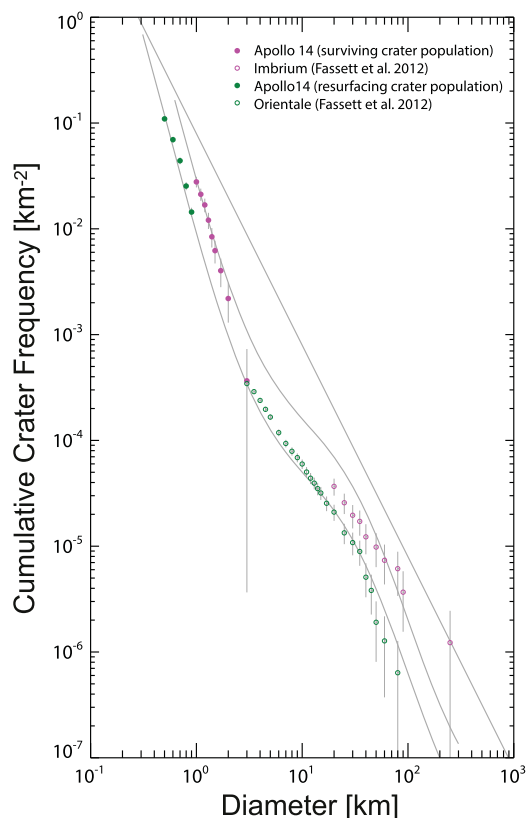
Figure 4. Crater statistics for the Apollo 14 landing site in comparison to Imbrium and Orientale. Crater size–frequency distributions (CFSD) for the craters observed in the Landing-Site Unit are as shown in Figure 3, and those of Imbrium basin and Orientale basin are as derived by Fassett et al. (2012); error bars show standard deviation. Using isochrones representing the crater frequencies observed at the Apollo 14 site of the surviving and resurfacing crater populations, we can show that the latter is very well in agreement with the measurement by Fassett et al. (2012) for Orientale, and the surviving population also matches the Imbrium relative age.

4. Implications for the Chemical Evolution of the Moon

Imbrium basin ejecta materials, often synonymous with the Fra Mauro formation, allegedly link temporally and compositionally with so-called KREEP-enriched samples (Warren & Wasson 1979; Warren 1985). KREEP-rich materials (lunar materials rich in K (potassium), REE (rare earth elements), P (phosphorus), and other incompatible, heat-producing elements such as Th) originated from a magma residuum layer that may have resulted from the differentiation and crystallization of a hypothetical lunar magma ocean (Warren 1985). KREEP-rich materials are thus a late-stage by-product of the formation of the widespread feldspar-rich anorthositic lunar crust and the mafic to ultramafic mantle. This postulated urKREEP layer (Warren & Wasson 1979) may have caused the longevity of volcanic activity in the area of the Oceanus Procellarum. Its chemical fingerprint is manifested in lunar samples at several landing sites, including the Apollo 14 site.

Potassium abundance correlates with thorium (e.g., Gillis et al. 2004, and references therein). Thorium maps therefore can be used to trace the abundance of KREEP-rich materials (Hawke & Head 1978). Globally, the maxima of the lunar thorium abundance map (Lawrence et al. 1998) coincide with a number of midsized (5–20 km in diameter) young craters and their ejecta in the Procellarum KREEP Terrane. Some ejecta of these midsized craters may have reached the Apollo 14 site.

However, interior and ejecta of the about 90 km diameter crater Copernicus show a rather low thorium content (Figure 5), which has been suggested to be due to the feldspathic composition of Copernicus ejecta (Pieters et al. 1985). On the contrary, Chang'e 5 basalt samples returned from the Oceanus Procellarum near the Mairan high-Th anomaly (Figure 5) lack the KREEP signature (Tian et al. 2021). The spectral signature of large parts of the highlands, including the Orientale basin and its interior fill, show even lower thorium content (Figure 5). Since all sample rocks that do not clearly identify as mare basalts show a KREEP component, we consider neither thorium nor KREEP enrichment to be a reliable discriminator between Orientale and Imbrium ejecta. When using remote sensing and comparing rock samples, trace element abundances can only be linked by proxies. Many samples, such as old alien stray boulders (e.g., at the Apollo 15 site; see Section 3.5) and those collected at other highland landing sites where Orientale ejecta was deposited (Apollo 16 and 17 and Luna 20; see Table A2), also include KREEP-enriched materials with ages of ∼3.92 Ga.

Apollo 14 breccia with ages between 4.31 ± 0.17 Ga and 3.94 ± 0.03 Ga show various degrees of KREEP enrichment (Warren & Wasson 1979; Hui et al. 2013). All rocks with ages of around 3.92 ± 0.06 Ga, now classified based on grain size as highland impact melt (Lofgren 1977; Hui et al. 2011, 2013; Nemchin et al. 2017; summarized in Table A3) and most found as fragments in different types of breccia, were originally categorized as KREEP-rich basalts. This calls for caution when using KREEP enrichment as a classification for the rock type and source, because it is not clear whether these samples formed as a result of a volcanic or an impact event (feldspathic basalt vs. impact melt). Thus, this sample characteristic exclusively is unsuitable for constraining chronostratigraphic anchors of the Moon.

5. Implications for the Lunar Chronostratigraphy

Our investigation comprises mapping of a unit representative of the samples collected at the Apollo 14 landing site, and for the first time combined with spectral and morphological analyses. We provide a new and more reliable crater frequency measurement to update the calibration of the lunar cratering chronology model. We propose a new stratigraphic relationship for the Apollo 14 landing site, between Imbrium and Orientale basins, with the topmost layer being the ejecta of the younger (and last) Orientale basin and not material from Imbrium basin. This interpretation is supported by spectral data and crater densities. Samples excavated by and collected near the rim of Cone crater could potentially have derived from Imbrium, but based on spectral affinity of the samples and age spread, it is more likely that no Imbrium ejecta were sampled at the Apollo 14 landing site. The impact melt breccia are therefore the ejecta of Orientale. Thus, the age of 3.922 ± 0.012 Ga (Nemchin et al. 2021) defines rather the timing of the Orientale formation. The observations presented here and the sample assignment to a single basin formation event (instead of multiple basin formation events) challenge the postulate of a lunar terminal cataclysm or conditions for a "Late Heavy Bombardment."

Compared to the commonly quoted ages (Ryder & Wood 1977; Stöffler et al. 2006) for the Imbrium and Orientale basins, we recommend revising the age for Orientale (previously suggested formation at 3.72 Ga; Stöffler et al. 2006) by increasing it by about 200 million years. This puts the Orientale basin formation at the recorded onset of mare volcanism rather
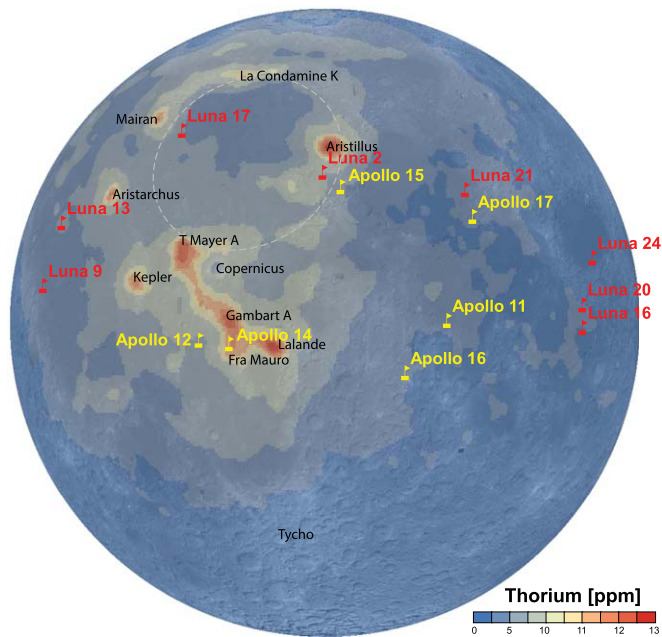
Figure 5. Nearside map of the Moon showing the thorium (Th) content. The Apollo 14 landing site features high values of Th. Peak values correlate with impact sites of young craters (shown by their names in the map) with extensive rayed ejecta patterns in the crater diameter range of 5–20 km. No high thorium content correlates with the impact sites of Copernicus or Tycho craters, both prominent rayed impact structures on the lunar nearside. Elevated Th abundance is observable within the entire region of Oceanus Procellarum and most mare units in its vicinity. The light-gray dashed line marks the suggested edge of the Imbrium basin.

than at some intermediate time before the peak of recorded activity. Given the 200-million-year shift, we predict that the Imbrium basin formed at about 4.12 Ga. Given the superposed crater densities for Orientale and Imbrium (Figure 3 or Figure 4), indicating a cratering rate difference of a factor of three, it is clear that the small-body population at 3.92 Ga ago was less numerous by a factor of three. Consequently, the contemporaneous impactor flux and all derived fluxes for other solar system bodies are lower than in previous studies (Stadermann et al. 1991 Basaltic Volcanism Study Project 1981; Neukum 1983; Wilhelms 1987; Neukum et al. 2001; Stöffler et al. 2006; Fassett et al. 2012; Robbins 2014). This raises the chance of an earlier onset of life on Earth and perhaps also on Mars.

6. Summary

Our results imply a fundamental revision of the temporal surface evolution of the Moon: Considering the complex histories of Apollo 14 samples, the evolution of highland crust near the impact site of Orientale is consequently also complex. Therefore, the lunar thermal history models and timescales must be revised in such a way that the feldspathic highland crust underwent significantly more and later thermal modifications than previously thought. This can account for the apparent resurfacing and emplacement of the observed lunar so-called intercrater (Strom 1977) or, as others have suggested, so-called light plains (Meyer et al. 2016). Since the lunar surface is the solar system's stencil for cratering statistics, our observations enforce a radical change of the cratering chronology model calibration, and the surface ages of other planetary bodies derived by previous crater statistics need revision.

Appendix
Supplementary Tables

We evaluated crater statistics, estimated stratigraphic columns from expected basin ejecta accumulation at several landing sites, and collected relevant sample ages. For the crater size-frequency measurements, we created two image mosaics using high-resolution images; the image numbers are listed accordingly in Table A1. The estimated stratigraphic columns differ in layer thicknesses for different parameters; a comparison is compiled in

Table A1
Image Data Used for the Mosaics

Evening TC Images	Morning TC Images
TCO_MAPe04_N00E339S03E342SC	TCO_MAPm04_N00E339S03E342SC
TCO_MAPe04_N00E342S03E345SC	TCO_MAPm04_N00E342S03E345SC
TCO_MAPe04_N00E345S03E348SC	TCO_MAPm04_N00E345S03E348SC
TCO_MAPe04_S03E339S06E342SC	TCO_MAPm04_S03E339S06E342SC
TCO_MAPe04_S03E342S06E345SC	TCO_MAPm04_S03E342S06E345SC
TCO_MAPe04_S03E345S06E348SC	TCO_MAPm04_S03E345S06E348SC
TCO_MAPe04_S06E339S09E342SC	TCO_MAPm04_S06E339S09E342SC
TCO_MAPe04_S06E342S09E345SC	TCO_MAPm04_S06E342S09E345SC
TCO_MAPe04_S06E345S09E348SC	TCO_MAPm04_S06E345S09E348SC

Table A2
Comparison of Ejecta Thickness Estimates at the Apollo 14 Landing Site for Different Scaling Laws (Housen et al. 1983; Fassett et al. 2011; Zhu et al. 2015)

	This Study ($h = 0.21$)	This Study ($h = 1$)	Fassett et al. (2011) ($h = 1$)	Zhu et al. (2015) ($h = 1$)[*]	Zhu et al. (2015) ($h = 1$)[+]	Housen et al. (1983) ($h = 1$)
SOUTH POLE–AITKEN	145	305	341	249	295	526
NUBIUM	755	594	623	589	697	852
MENDEL-RYDBERG	12	9	11	5	6	20
HUMORUM	299	270	292	244	288	423
SERENITATIS	111	110	123	89	106	191
SMYTHII	9	9	11	6	7	19
NECTARIS	67	64	73	49	58	117
CRISIUM	39	43	50	32	37	84
IMBRIUM	519	683	727	646	763	1024
SCHRÖDINGER	<0.5	<0.5	<0.5	<0.5	<0.5	1
ORIENTALE	27	27	32	19	23	54
Σ	1983	2114	2283	1928	2280	3311

Note. All numeric values are in units of meters. The property h denotes the scaling exponent in the basin depth–diameter relationship used to estimate the basin volume. For the work of Zhu et al. (2015), estimates are given for the two different pre-impact target crustal thicknesses, which these authors used in their Orientale formation model: [*]40 km, [+]60 km.

Table A3
List of Apollo 14 Sample Ages (Not Claiming Completion)

Sample	Type	System	Age	Error	Reference	Correction
14078,2	*impact melt*	^{87}Rb/^{87}Sr	*3760*	*20*	8	Age corrected using ^{87}Rb decay constant value (2)
14001,7,3	*impact melt*	^{87}Rb/^{87}Sr	*3870*	*30*	9	Ages corrected by Hui et al. (6) applying ^{87}Rb decay constant value after (12)
14150,7,2	*impact melt*	^{87}Rb/^{87}Sr	*3840*	*40*	10	
14150,7,3	*impact melt*	^{87}Rb/^{87}Sr	*3880*	*20*	10	
14276	*impact melt*	^{87}Rb/^{87}Sr	*3860*	*20*	11	
14073	*impact melt*	^{87}Rb/^{87}Sr	*3860*	*20*	11	
14310,101	*impact melt*	^{40}Ar/^{39}Ar	*3790*	*220*	13	Age corrected for ^{40}K decay constant (1)
14310,101	*impact melt*	^{40}Ar/^{39}Ar	*3870*	*40*	14	No step-heating data, age is corrected only for ^{40}K decay constant and monitor age (1), see also below.
14310	*impact melt*	^{87}Rb/^{87}Sr	*3850*	*20*	11	Ages corrected by Hui et al. (6) applying ^{87}Rb decay constant value after (12)
14310,118	*impact melt*	^{87}Rb/^{87}Sr	*3920*	*60*	7	
14083,35,1	clast-rich impact melt breccia	^{207}Pb/^{204}Pb	3920	20	3	in situ on zircon found within matrix of K-feldspar clast-1,2 in Section 14083,35
14083,35,2		^{207}Pb/^{204}Pb	3923	28	3	
14303,49		^{207}Pb/^{204}Pb	3920	13	3	clast-1 in Section 14303,49
14321,xx	*Group A basalt*	^{87}Rb/^{87}Sr	*4260*	*100*	Age Averages	Ages corrected by Hui et al. (6) from references therein for each of the three Apollo 14 basaltic groups applying ^{87}Rb decay constant value after (12)
	Group B basalt	^{87}Rb/^{87}Sr	*4040*	*60*		
14053	*Group C basalt*	^{87}Rb/^{87}Sr	*3940*	*30*	11	
14053,34	*basalt in breccia*	^{40}Ar/^{39}Ar	*4016*	*90*	14	For these ages there were no step-heating data reported to enable complete reevaluation of the sample age including their replotting. The correction was solely done on the age reported by (14) and extracted from the plateau and high-temperature heating steps. The correction of these ages takes into account the update in the ^{40}K decay constants and the age of the ^{39}Ar monitor (1).
14152,1,1	*medium grained ophi-tic soil*	^{40}Ar/^{39}Ar	*3913*	*110*		
14152,1,2		^{40}Ar/^{39}Ar	*3841*	*60*		
		^{40}Ar/^{39}Ar	*3882*	*90*		
14167,6,1	*rock chips from soil samples*	^{40}Ar/^{39}Ar	*3882*	*40*		
14167,6,3		^{40}Ar/^{39}Ar	*3923*	*60*		
14167,6,4		^{40}Ar/^{39}Ar	*3813*	*40*		
14167,6,7		^{40}Ar/^{39}Ar	*3913*	*40*		
14192,1,1		^{40}Ar/^{39}Ar	*4016*	*—*		
14193,2,1		^{40}Ar/^{39}Ar	*3913*	*110*		
14257,12,1		^{40}Ar/^{39}Ar	*3964*	*70*		
14257,12,3		^{40}Ar/^{39}Ar	*3585*	*130*		
14063,207	*Granulitic clast*	^{40}Ar/^{39}Ar	*4114*	*30*	15	Age corrected for ^{40}K decay constant (1)
14063,234	*Cataclastic noritic anor-thosite clast*	^{40}Ar/^{39}Ar	*3970*	*20*		
14079,3	*Feldspathic basalt*	^{40}Ar/^{39}Ar	*3888*	*30*		
14140,12	*Basaltic regolith fragment*	^{40}Ar/^{39}Ar	*4083*	*20*		
14179,11	*Anorthosite separates*	^{40}Ar/^{39}Ar	*4083*	*60*		
14434,3	*Shocked cataclastic grabbronorite*	^{40}Ar/^{39}Ar	*3816*	*110*		
14305	Zircon grains in breccias	^{207}Pb/^{206}Pb	3926, 4058–4300		4,5	For the detailed interpretation and error ranges please see references (4,5)
14306		^{207}Pb/^{206}Pb	3926, 4078–4349			
14314		^{207}Pb/^{206}Pb	3929, 3936-4346			
14321		^{207}Pb/^{206}Pb	3943–4325			

Note. We base our age interpretation on information of samples printed in nonitalics and exclude all entries printed in italics, because the latter are, compared to the original publication, corrected ages as described in the text and in the "Correction" column.

Reference (1) Renne et al. 2011; (2) Nebel et al. 2011; (3) Nemchin et al. 2017; (4) Thiessen et al. 2019; (5) Snape et al. 2016; (6) Hui et al. 2013; (7) Compston et al. 1972; (8) McKay et al. 1978; (9) Papanastassiou & Wasserburg 1971; (10) McKay et al. 1979; (11) Wasserburg & Papanastassiou 1971; (12) Rotenberg et al. 2012; (13) Schaeffer & Schaeffer 1977; (14) Husain et al. 1972. (15) Turner et al. 1973.

Table A2. Furthermore, for the discussion on sample ages, we surveyed the literature, updated older sample ages according to modern decay constants, and present a list of modern and updated ages for Apollo 14 samples in Table A3.

ORCID iDs

Stephanie C. Werner ● https://orcid.org/0000-0001-5704-0909
Benjamin Bultel ● https://orcid.org/0000-0002-7084-9574

References

Arvidson, R., Drozd, R. J., Hohenberg, C. M., et al. 1975, Moon, 13, 67
Basaltic Volcanism Study Project 1981, Basaltic Volcanism on the Terrestrial Planets (New York: Pergamon)
Chao, E. C. T., Minkin, J. A., & Best, J. B. 1972, LPSC, 3, 645
Compston, W., Vernon, M. J., Berry, H., et al. 1972, LPSC, 3, 1487
Dibb, S., & Kiefer, W. 2015, LPSC, 46, 1677
Fassett, C. I., Head, J. W., Kadish, S. J., et al. 2012, JGRE, 117, E00H06
Fassett, C., Head, J., Smith, D., et al. 2011, GeoRL, 38, L17201
Fernandes, V. A., & Artemieva, N. 2012, LPSC, 43, 1367
Fernandes, V. A., Fritz, J., Weiss, B., et al. 2013, M&PS, 48, 241
Fernandes, V. A., Werner, S. C., & Fritz, J. P. 2014, LPI Contribution, 1800, 5011
Gancarz, A. J., Albee, A. L., & Chodos, A. A. 1972, E&PSL, 16, 307
Gault, D. E. 1970, RaSc, 5, 273
Gilbert, G. K. 1893, Phil. Soc. Washington Bull, 12, 452
Gillis, J. J., Jolliff, B. L., & Korotev, R. L. 2004, GeCoA, 68, 3791
Green, R. O., Pieters, C., Mouroulis, P., et al. 2011, JGRE, 116, E00G19
Haruyama, J., Matsunaga, T., Ohtake, M., et al. 2008, E&PS, 60, 243
Haskin, L. A., Moss, B. E., & McKinnon, W. B. 2003, M&PS, 38, 13
Hawke, B. R., & Head, J. W. 1978, LPSC, 9, 3285
Housen, K. R., Schmidt, R. M., & Holsapple, K. A. 1983, JGR, 88, 2485
Housen, K. R., Wilkening, L. L., Chapman, C. R., et al. 1979, Icar, 39, 317
Hui, H., Neal, C. R., Shih, C.-Y., et al. 2013, E&PSL, 373, 150
Hui, H., Oshrin, J. G., & Neal, C. R. 2011, GeCoA, 75, 6439
Husain, L., Schaeffer, O. A., Funkhouser, J., et al. 1972, LPSC, 3, 1557
Kneissl, T., van Gasselt, S., & Neukum, G. 2011, P&SS, 59, 1243
Kreslavsky, M. A., & Head, J. W. 2012, JGRE, 117, E00H24
Lawrence, D. J., Feldman, W. C., Barraclough, B. L., et al. 1998, Sci, 281, 1484
Levenberg, K. 1944, QApMa, 2, 164
Lofgren, G. E. 1977, LPSC, 8, 2079
Longhi, J., Walker, D., & Hays, J. F. 1972, LPSC, 3, 131
Ludwig, K. R. 2003, Isoplot 3.00: A Geochronological Toolkit for Microsoft Excel, Special Publication/Berkeley Geochronology Center; No. 4 70
Marquardt, D. 1963, SIAM Journal on Applied Mathematics, 11, 431
McGetchin, T., Settle, M., & Head, J. W. 1973, E&PSL, 20, 226
McKay, G. A., Wiesmann, H., Bansal, B. M., et al. 1979, LPSC, 10, 181
McKay, G. A., Wiesmann, H., Nyquist, L. J., et al. 1978, LPSC, 9, 661
Merle, R. E., Nemchin, A. A., Grange, M. L., et al. 2014, M&PS, 49, 2241
Meyer, H. M., Denevi, B. W., Boyd, A. K., et al. 2016, Icar, 273, 135
Michael, G., & Neukum, G. 2010, E&PSL, 294, 223
Moore, H. J., Hodges, C. A., & Scott, D. H. 1974, LPSC, 5, 71

Neal, C. R., & Kramer, G. Y. 2006, AmMin, 91, 1521
Nebel, O., Scherer, E. E., & Mezger, K. 2011, E&PSL, 301, 1
Nemchin, A. A., Jeon, H., Bellucci, J. J., et al. 2017, GeCoA, 217, 441
Nemchin, A. A., Long, T., Jolliff, B. L., et al. 2021, ChEG, 81, 125683
Neukum, G. 1983, Meteoritenbombardement und Datierung planetarer Oberflächen, Habilitation Dissertation for Faculty Membership, Universität München
Neukum, G., Ivanov, B. A., & Hartmann, W. K. 2001, in Chronology and Evolution of Mars, ed. R. Kallenbach, J. Geiss, & W. K. Hartmann (Dordrecht: Kluwer), 55
Neukum, G., Koenig, B., & Arkani-Hamed, J. 1975, Moon, 12, 201
Neumann, G., Zuber, M. T., Wieczorek, M. A., et al. 2015, SciA, 1, e1500852
Oberbeck, V. R. 1975, RvGSP, 13, 337
Oberbeck, V. R., Morrison, R. H., Hörz, F., et al. 1974, LPSC, 5, 111
Ogawa, Y., Matsunaga, T., Nakamura, R., et al. 2011, GeoRL, 38, L17202
Papanastassiou, D. A., & Wasserburg, G. J. 1971, E&PSL, 12, 36
Petro, N. E., & Pieters, C. M. 2004, JGR, 109, E06004
Petro, N. E., & Pieters, C. M. 2006, JGR, 111, E09005
Pieters, C. M., Adams, J. B., & Mouginis-Mark, P. J. 1985, JGR, 90, 12393
Pike, R. J. 1974, E&PSL, 23, 265
Prieur, N. C., Rolf, T., Luther, R., et al. 2017, JGRE, 122, 1704
Renne, P. R., Mundil, R., Balco, G., et al. 2011, GeCoA, 75, 5097
Robbins, S. J. 2014, E&PSL, 403, 188
Rolf, T., Zhu, M.-H., Wünnemann, K., et al. 2017, Icar, 286, 138
Rotenberg, E., Davis, D. W., Amelin, Y., et al. 2012, GeCoA, 85, 41
Ryder, G., & Wood, J. A. 1977, LPSC, 8, 655
Schaeffer, G. A., & Schaeffer, O. A. 1977, LPSC, 8, 2253
Simonds, C. H., Phinney, W. C., Warner, J. L., et al. 1977, LPSC, 8, 1869
Snape, J. F., Nemchin, A. A., Grange, M. L., et al. 2016, GeCoA, 174, 13
Snape, J. F., Nemchin, A. A., Whitehouse, M. J., et al. 2019, GeCoA, 266, 29
Stadermann, F. J., Heusser, E., Jessberger, E. K., et al. 1991, GeCoA, 55, 2339
Stöffler, D., Ryder, G., Ivanov, B. A., et al. 2006, RvMG, 60, 519
Strom, R. G. 1977, PEPI, 15, 156
Swindle, T. D., Spudis, P. D., Taylor, G. J., et al. 1991, LPSC, 21, 167
Tera, F., Papanastassiou, D. A., & Wasserburg, G. J. 1973, LPSC, 4, 723
Tera, F., Papanastassiou, D. A., & Wasserburg, G. J. 1974, E&PSL, 22, 1
Thiessen, F., Nemchin, A. A., Snape, J. F., et al. 2019, M&PS, 54, 1720
Tian, H. C., Wang, H., Chen, Y., et al. 2021, Natur, 600, 59
Turner, G., Cadogan, P. H., & Yonge, C. J. 1973, LPSC, 4, 1889
Turner, G., Huneke, J. H., Podosek, F. A., et al. 1971, E&PSL, 12, 19
Walker, D., Grove, T. L., Longhi, J., et al. 1973, E&PSL, 20, 325
Warren, P. H. 1985, AREPS, 13, 201
Warren, P. H., & Wasson, J. T. 1979, RvGeo, 17, 73
Wasserburg, G. J., & Papanastassiou, D. A. 1971, E&PSL, 13, 97
Watkins, J. S., & Kovach, R. L. 1972, Sci, 175, 1244
Wetherill, G. W. 1975, LPSC, 6, 1539
Wieczorek, M. A., & Zuber, M. T. 2001, JGR, 106, 27853
Wilhelms, D. 1987, The Geologic History of the Moon, Professional Paper, 1348, USGS
Wu, B., Wang, Y., Lin, T. J., et al. 2019, Icar, 333, 343
Xiao, Z., Ding, C., Xie, M., et al. 2021, GeoRL, 48, e90935
Xiao, Z., & Werner, S. C. 2015, JGRE, 120, 2277
Xie, M., Liu, T., & Xu, A. 2020, JGRE, 125, e06113
Xie, M., & Zhu, M.-H. 2016, E&PSL, 440, 71
Zhang, X.-Y., Ouyang, Z.-Y., Zhang, X.-M., et al. 2016, RAA, 16, 115
Zhu, M.-H., Wünnemann, K., & Potter, R. 2015, JGRE, 120, 2118